OPTICA

High-sensitivity distributed quantum sensing of multimodal parameters

Jingxu Ma,[1,†] Jieli Yan,[1,†] Shaocong Liang,[1] Zhihui Yan,[1,2,*] Xiaojun Jia,[1,2,3] Changde Xie,[1,2] and Kunchi Peng[1,2]

[1]State Key Laboratory of Quantum Optics Technologies and Devices, Institute of Opto-Electronics, Shanxi University, Taiyuan 030006, China
[2]Collaborative Innovation Center of Extreme Optics, Shanxi University, Taiyuan 030006, China
[3]jiaxj@sxu.edu.cn
[†]The authors contributed equally to this work.
*zhyan@sxu.edu.cn

Received 13 October 2025; revised 24 December 2025; accepted 24 February 2026; published 18 March 2026

Quantum sensing has emerged as a promising solution for precision measurement, and distributed quantum sensing enables multiple parameters to be measured across a network. Pushing distributed quantum sensing from the single to multimodal parameters is crucial for a complete and deep understanding of a complex system. To address this challenge, we have devised a high-sensitivity distributed quantum sensing of the multimodal parameters with a continuous-variable multipartite Greenberger–Horne–Zeilinger entangled state. All the sensors are equipped with Mach–Zehnder interferometers to couple the lasers with entangled modes. In such a quantum network, not only joint but also individual measurements of radio frequency phases and amplitudes as well as ultrasonic vibration signals are achieved beyond the standard quantum limit, showcasing the quantum Fisher information of the order of 10^{16}. These results render multimodal parameters a promising contender in quantum metrology. © 2026 Optica Publishing Group under the terms of the Optica Open Access Publishing Agreement

https://doi.org/10.1364/OPTICA.581723

1. INTRODUCTION

Quantum sensing has played an essential role in the development of precision measurement and its applications in modern quantum technology [1]. In recent years, significant progress in quantum sensing has been achieved in single-parameter estimation [2–6], using squeezed [7–11] and entangled states [12,13]. Furthermore, the growing complexity in practical scenarios has facilitated the exploration of a variety of fascinating applications, such as polarization microscopy [14], qubit tomography [15], multidimensional field estimation [16], imaging [17–20], and biosensing [21–23]. This trend has driven increasing interest in ultrasensitive measurements of more parameters.

Bringing quantum sensing from single-parameter to multi-parameter regimes—which requires a sufficiently large quantum resource—substantially boosts sensitivity by increasing the number of sensors and utilizing quantum correlations [24–26]. A plethora of applications relies on distributed quantum sensing to undertake measurement tasks. The entanglement-enhanced distributed sensing scheme is proposed by dividing a squeezed-vacuum state among multiple nodes with a beam-splitter array [27], and notable experimental advances have been made in distributed quantum sensing of multiple phases [28–32]. In the reconfigurable entangled radio frequency sensor network, distributed quantum sensing advantage empowered by continuous-variable (CV) multipartite entanglement has been demonstrated [33,34]. However, the existing schemes remain constrained to a single modal parameter, which faces limitations in complex and multi-source signal environments.

Distributed quantum sensing of multimodal parameters is in high demand, as information acquisition and processing involving diverse modalities of optical, acoustic, electric, and magnetic signals are opening new paradigms for a deeper and more comprehensive understanding of the measured systems [35–41]. The multimodal technologies play a key role in biological sensing and imaging, such as multimodal generative AI for medical image interpretation [42], neural modulation and sensing [43], multimodal brain–computer interfaces [44], and dark matter searches [45,46]. In quantum sensing, it is highly demanded to acquire information more accurately by measuring more modal parameters. Furthermore, joint measurement of different parameters can evaluate the global information of analytes, whereas the individual measurement provides the local information. So far, it is challenging to completely obtain the multimodal parameters with high sensitivity due to the restrictions of the Heisenberg uncertainty principle [47,48]. Particularly, both global and local information are required for deeply understanding the system.

In this work, we develop a metrology paradigm for high-sensitivity distributed quantum sensing of multimodal parameters, including quadrature amplitude-related radio frequency amplitudes besides quadrature phase-related radio frequency phases and ultrasonic vibrations. Such advances are attributed to key quantum-classical hybrid technology to integrate the classical

Mach–Zehnder interferometers (MZIs) with the Greenberger–Horne–Zeilinger (GHZ) entangled network. First, with the GHZ entangled optical fields as an efficient resource, the measurement information can be increased by simultaneously reading out two conjugate parameters. In this way, the quantum correlation noises are squeezed, and the conjugate parameters act as estimators of independent signals. Second, it pushes distributed quantum sensing from the single modal to multimodal parameters, such as sonic vibration [49] and radio frequency amplitude and phase [50], which are crucial for a complete and deep understanding of nature. The radio frequency phase and amplitude signals, as well as ultrasonic vibration signals, can be jointly measured surpassing the standard quantum limit (SQL). Third, not only joint but also individual measurements of multimodal signals can be achieved for complete information. Furthermore, the quantum network can be scalable to more sensors and robust against the distribution losses, enabled by the use of CV quantum states. Fourth, the classical MZIs can enhance signals by coupling the high-power lasers into the interferometer, while GHZ entangled state can qualitatively increase the measurement information by simultaneously reading out two conjugate parameters beyond the SQL. For two radio frequency phase signals, three radio frequency amplitude signals, and two ultrasonic vibration signals, we achieve high-sensitivity multimodal quantum sensing. The quantum correlation noises are 2.4 dB below SQL with a distribution loss of 0.24. The quantum Fisher information (QFI), which quantifies the ultimate sensitivity for a given quantum state, i.e., quantum Cramér–Rao bounds (QCRB), reaches 1.83×10^{16} in this quantum network. The high-sensitivity sensing of ultrasonic vibration is key for photo-acoustic imaging, while the radio frequency parameters can be used to image biological tissue and tumors due to the sensitive response of radio frequency on water. The sensitivity for multimodal parameters can be further improved by using joint measurements of multiparameters with a specific weight structure. These results demonstrate the quantum-enhanced multimodal sensing with high sensitivity, representing a significant evolution in precision measurement paradigms and the development of high-performance quantum networks.

2. PRINCIPLE OF DISTRIBUTED QUANTUM SENSING OF MULTIMODAL PARAMETERS

CV quantum states have advantages in deterministic generation, manipulation, and measurement [51–54]. Quantum dense metrology is particularly promising, showing the joint measurement of a pair of non-commuting parameters by utilizing Einstein–Podolsky–Rosen entanglement, and serving as a building block for distributed quantum sensing of multimodal parameters [55,56]. The precision measurement of multiple parameters across different modalities is essential for multimodal quantum sensing to achieve a deeper understanding of the system. Figure 1 demonstrates the GHZ entanglement-enhanced measurement of multiple radio frequency phases and amplitude and ultrasonic vibration signals. The quadrature amplitude $\hat{X}$ and phase $\hat{Y}$ of the optical field $\hat{a}$ can be expressed using the creation and annihilation operators of the optical field as $\hat{X} = (\hat{a} + \hat{a}^\dagger)/\sqrt{2}$ and $\hat{Y} = i(\hat{a}^\dagger - \hat{a})/\sqrt{2}$. The quantum states can be used for the quantum-enhanced sensing of a single parameter. However, the quadrature operators $\hat{X}$ and $\hat{Y}$ constitute a pair of non-commuting observables, satisfying the commutation relation $[\hat{X}, \hat{Y}] = i$.

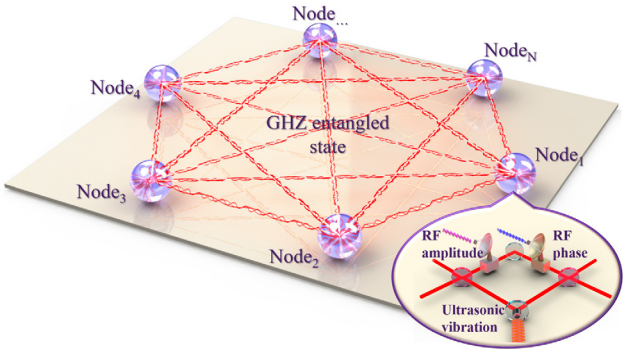

Fig. 1. Schematic diagram of distributed quantum sensing of multimodal parameters. The multiple nodes are fully interconnected through a GHZ entangled state. Multimodal parameters including the radio frequency amplitude and phase and ultrasonic vibration signals can be detected by the node sensors, which enables entanglement-enhanced measurements of multimodal parameters.

Consequently, it is impossible to simultaneously determine non-commuting observables, such as phase and amplitude of optical fields, with accuracy beyond the SQL due to the limitation imposed by the Heisenberg uncertainty principle. Beyond bipartite quantum entanglement for quantum dense metrology, a CV multipartite GHZ entangled state with nonlocal quantum correlations is employed for the joint measurement of multimodal parameters, achieving sensitivities surpassing the SQL.

In the quantum sensing network, all the sensors are coupled inside MZIs with strong coherent states injected to achieve high sensitivity. Three types of modal parameters—the amplitude of radio frequency signals, the phase of radio frequency signals, and vibrations of ultrasonic signals—are sensed via electro-optic transducers (EOTs) and piezoelectric transducers (PZTs), respectively. First, the M-mode product state of squeezed states is used as the input state, denoted as $|\psi_{\text{in}}\rangle = |\psi_1\rangle \otimes |\psi_2\rangle \otimes \cdots \otimes |\psi_M\rangle$. After coupling on the first beam splitter network (BSN1), the multipartite GHZ state is generated to construct the quantum sensing network (see Supplement 1 for a detailed introduction). The multipartite GHZ state is an eigenstate with total momentum zero and all relative positions zero, and the correlation noises of the quadrature amplitudes and phases for the multipartite GHZ state are $\Delta^2\langle \hat{X}_1 + \hat{X}_2 + \cdots + \hat{X}_M \rangle = Me^{-2r}/2$, $\Delta^2\langle \hat{Y}_m - \hat{Y}_n \rangle = e^{-2r} (m \neq n;\ m, n = 1, 2, \cdots, M)$, where r denotes the squeezing factor. Subsequently, the multipartite GHZ entangled modes are distributed to connect all the multimodal sensors and squeeze the quantum correlation noises. The amplitude and phase of radio frequency signals and vibrations of ultrasonic signals are received by EOTs and PZTs. Each sensor is equipped with an MZI to couple high-power lasers with entangled modes. The destructive interference outputs of MZIs are injected into the second beam splitter network (BSN2), so that photodiode saturation is avoided and high phase-sensing power is permitted. Global Gaussian measurements are performed using balanced homodyne detectors (BHDs) to obtain the joint measurement results for multimodal quantum sensing. Joint measurement refers to estimating a linear combination of parameters to be measured. For the joint measurements, the estimated parameters include the joint radio frequency amplitude $\epsilon_1^J = \frac{\sum_{m=1}^{M} \epsilon_m}{M}$, the joint radio frequency phase $\theta_j^J = \frac{(M-j)\theta_j + \sum_{m=j+1}^{M-1} \theta_m}{2M-2j-1}$, and the joint ultrasonic

vibration $d_j^J = \frac{(M-j)d_j+\sum_{m=j+1}^{M-1} d_m}{2M-2j-1}$ $j = 1, \cdots, M-2$. The joint measurement sensitivity for the radio frequency amplitude signals at the Mth output port, along with the joint sensitivities for the radio frequency phase and ultrasonic vibration signals at the 2nd to Mth output ports, are given by (for more details, see Supplement 1)

$$\begin{aligned}\Delta\epsilon_1^J &= \sqrt{\frac{hc}{2MP\lambda e^{2r}}},\\ \Delta\theta_j^J &= \sqrt{\frac{(M-j)(M-j+1)hc}{2\,(2M-2j-1)^2\,P\lambda e^{2r}}},\\ \Delta d_j^J &= \frac{1}{4\pi}\sqrt{\frac{(M-j)(M-j+1)hc\lambda}{2\,(2M-2j-1)^2\,Pe^{2r}}},\end{aligned} \tag{1}$$

where h is the Planck constant, c is the light speed in a vacuum, P is the phase-sensing optical power, and λ is the wavelength. Quantum states enable all sensitivities to surpass the SQL, facilitating joint measurements of various modal signals. Furthermore, the sensitivities increase with a higher sensor count, greater phase-sensing power, and larger squeezing factors.

Furthermore, the individual measurement sensitivity refers to the sensitivity obtained after the joint measurement by performing post-processing on the BHD measurement results to extract the estimator of a particular local parameter. Individual measurement sensitivities for radio frequency phase and ultrasonic vibration signals at each sensor can be obtained with the post-processing, as follows:

$$\begin{aligned}\Delta\theta_j^I &= \sqrt{\frac{hc}{P\lambda e^{2r}}},\\ \Delta d_j^I &= \frac{1}{4\pi}\sqrt{\frac{hc\lambda}{Pe^{2r}}},\end{aligned} \tag{2}$$

where $j = 1, \cdots, M-1$. These results show multimodal quantum sensing of the phase and amplitude of radio frequency signals as well as vibrations of ultrasonic signals.

3. EXPERIMENTAL REALIZATION

A. Experimental Setup

The quantum sensing network is experimentally constructed to demonstrate distributed quantum sensing of multimodal parameters, as schematically illustrated in Fig. 2. In the first part of the non-classical light source, a continuous wave intracavity frequency-doubled tunable single-frequency Nd:YAP/LBO solid-state laser is used to generate a second harmonic wave at 540 nm as the pump light of the non-degenerate optical parametric amplifier (NOPA), and a fundamental wave at 1080 nm as the seed light of the NOPA, the input coherent state of the interferometer, and the local oscillator of BHD. Using two identical type-II phase-matched NOPAs for parametric down-conversion, the two generated beams of quadrature phase-squeezed light and one beam of quadrature amplitude-squeezed light are combined through BSN1 to produce a tripartite GHZ entangled state (see Supplement 1). The quadrature phase-squeezed and quadrature amplitude-squeezed fields generated by NOPA1 are interfered on a 2:1 beam splitter (BS). This results in the generation of two beams, which are denoted as $\hat{b}_1$ and $\hat{a}_1'$. Afterward, the phase-squeezed light generated by NOPA2 is combined with $\hat{a}_1'$ using a 1:1 BS. This gives rise to two additional beams, which are referred to as $\hat{b}_2$ and $\hat{b}_3$. The three resultant modes $\hat{b}_1$, $\hat{b}_2$, and $\hat{b}_3$ form a GHZ entangled state with 4.00 ± 0.21 dB below the SQL, which are allocated to three spatially separated sensors. In the second part for multimodal quantum sensing, each sensor is coupled into an MZI, which consists of two balanced BS. The entangled submodes of the GHZ state are coupled with intense coherent lights $\hat{c}_1$, $\hat{c}_2$, and $\hat{c}_3$ on the first BS. In the first and second quantum sensors, one arm of the MZI is driven by a 2.1 MHz sinusoidal signal applied to the PZT to introduce an ultrasonic vibration signal, and the other arm detects a radio frequency signal field. This signal field undergoes modulation of amplitude and phase by loading a

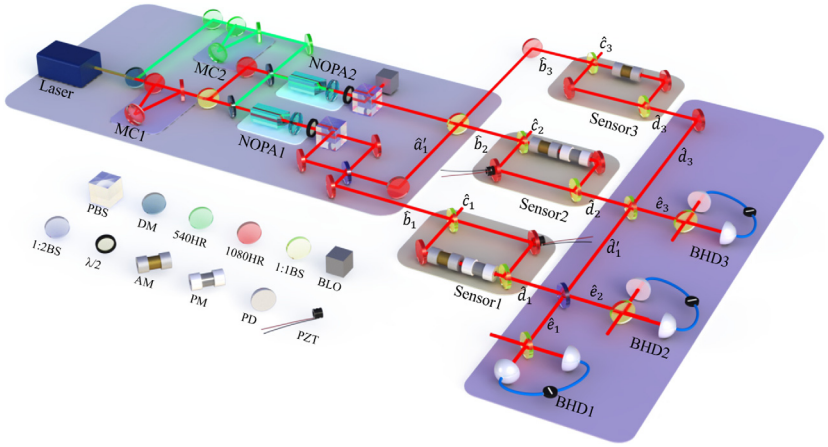

Fig. 2. Experimental setup for distributed quantum sensing of multimodal parameters using CV multipartite GHZ entanglement. Two NOPAs, together with beam splitters, are used to generate GHZ-entangled optical fields that couple all multimodal sensors. The phase and amplitude of radio frequency signals are detected by PMs and AMs, and vibrations of ultrasonic signals are received using PZTs. The multimodal signals are finally obtained by using three BHD-based global measurements. MC, mode-cleaner cavity; NOPA, non-degenerate optical parametric amplifier; PBS, polarizing beam splitter; DM, dichroic mirror; 540HR, highly reflective mirror for the 540 nm; 1080HR, highly reflective mirror for the 1080 nm; BLO, optical block; BS, beam splitter; $\lambda/2$, half–wave plate; PD, photodiode; AM, amplitude modulator; PM, phase modulator; and PZT, piezoelectric transducer.

2.8 MHz sinusoidal signal to the AM and PM. In the third sensor, only one arm of the MZI receives a 2.8 MHz sinusoidal signal via the AM. The phase-sensing power of the ultrasonic vibration signal is 600 μW, while the radio frequency signal has a power of 60 μW. The optical fields $\hat{d}_1$, $\hat{d}_2$, and $\hat{d}_3$ from the destructive interference ports of the interferometers are injected into the BSN2, consisting of 1:1 and 2:1 BSs. In the third part for measurement, the output states $\hat{e}_1$, $\hat{e}_2$, and $\hat{e}_3$ from BSN2 are detected by three sets of BHDs. The quadrature amplitude $\hat{X}$ of output state $\hat{e}_1$ is measured by the BHD. At the same time, the quadrature phase $\hat{Y}$ of output states $\hat{e}_2$ and $\hat{e}_3$ is measured by identical BHDs. The variance of the quadrature operator corresponds to the alternating current output of the BHD, which is recorded by the spectrum analyzer.

B. Experimental Results

The distributed quantum sensing of the amplitude and phase of radio frequency signals as well as the amplitude of ultrasonic signals is illustrated in Fig. 3. The losses in the two arms of the interferometer are $\varsigma_1 = 0.01$ and $\varsigma_2 = 0.002$, and the external losses outside the interferometer $\xi = 0.24$, which includes the loss due to interference imperfections $\xi_I = 0.073$, transmission loss $\xi_T = 0.13$, and detection loss $\xi_D = 0.06$. The entanglement-enhanced joint measurement can be realized due to the quantum correlation of the GHZ state. Figure 3(a) shows the joint measurement power spectrum of quadrature amplitudes of three 2.8 MHz radio frequency signals by using the first output state $\hat{e}_1$ of BSN2. The signal-to-noise ratio (SNR) is enhanced by 2.42 dB beyond the SQL, due to the quantum correlations of the GHZ state. Figure 3(b) shows the joint measurement power spectra of two ultrasonic vibration signals at 2.1 MHz and two radio frequency phase signals at 2.8 MHz at the second output state $\hat{e}_2$ of BSN2. With such a GHZ entangled network, we observe that the SNR is enhanced by 2.43 dB beyond the SQL. We then assessed radio frequency sensing using the entangled sensing network. The red and green circles in Figs. 3(c), 3(d) show the joint measurement results of the radio frequency amplitudes and phases from BHD1 and BHD2, respectively. The homodyne data of the joint radio frequency amplitudes are obtained, when the radio frequency amplitude is swept from 170 to 390 mV. In Fig. 3(c), the quantum sensor network (blue shaded region) exhibits a quantum sensing advantage of 2.4 dB in correlation variance compared with the classical sensor network (pink shaded region). Alternatively, the homodyne signals marked as circles in Fig. 3 (d) show a clear sinusoidal behavior with the green circles and corresponding correlation variances in shaded region, as the radio frequency phase is scanned from 0 to 2π in $\pi/9$ steps. The result exhibits the advantage of the entangled network with approximately 2.5 dB noise suppression below the SQL.

Furthermore, the individual measurement sensitivity of the radio frequency phase and ultrasonic vibration signals can be obtained to extract the individual parameters by performing post processing the BHD results, as illustrated in Fig. 4. Quantum-enhanced individual measurement is achieved because the GHZ entangled state is transformed back to the individual squeezed states. Figure 4(a) displays the power spectra of the individual measurements of radio frequency phase signal θ_1 and ultrasonic vibration signal d_1, which are obtained by post processing of the measurement outputs $\hat{e}_2$ and $\hat{e}_3$. Figure 4(b) displays the power spectra of radio frequency phase signal θ_2 and ultrasonic vibration signal d_2 by using the third output state $\hat{e}_3$. The SNRs of radio frequency phases and ultrasonic vibrations in the entangled network are improved by 2.53 and 2.48 dB compared to the SQL, respectively. With a similar approach of Figs. 3(c), 3(d), Figs. 4(c) and 4(d) show the individual radio frequency phases. It can be seen

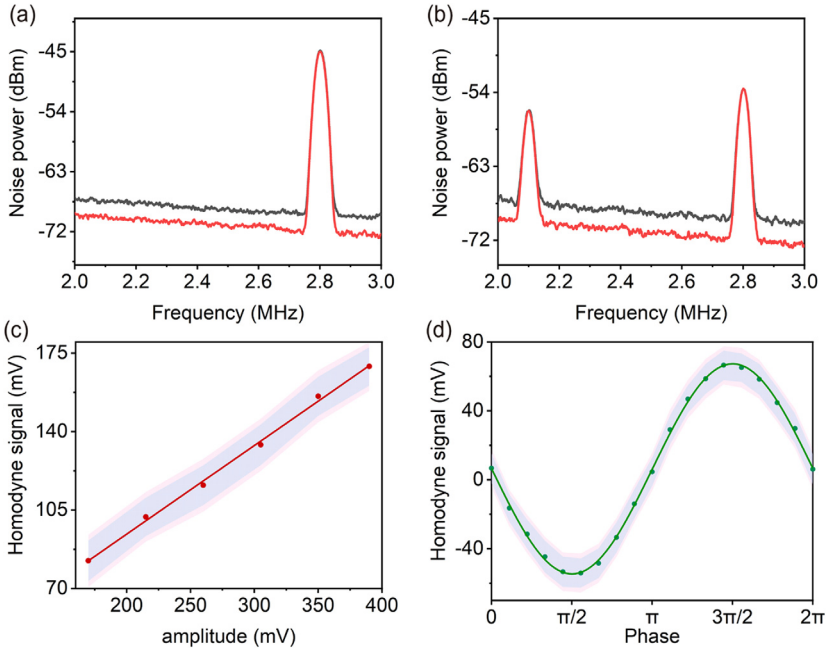

Fig. 3. (a, b) Experimental results of the joint measurements of radio frequency amplitude signals ϵ_1^J (a), the vibrations of ultrasonic signals d_1^J at 2.1 MHz and phase of radio frequency signals θ_1^J at 2.8 MHz (b). The black and red traces correspond to the noise power based on classical and entangled schemes, respectively. The measurement parameters of the spectrum analyzer: video bandwidth, 6.8 Hz; resolution bandwidth, 4.3 kHz. (c, d) The joint quadratures of radio frequency signals at the BHD1 and BHD2 under different radio frequency amplitudes and phases, respectively. Circles, experimental data; curves, data fits; shaded area, estimation uncertainties for entangled (blue) and classical (pink) sensor networks.

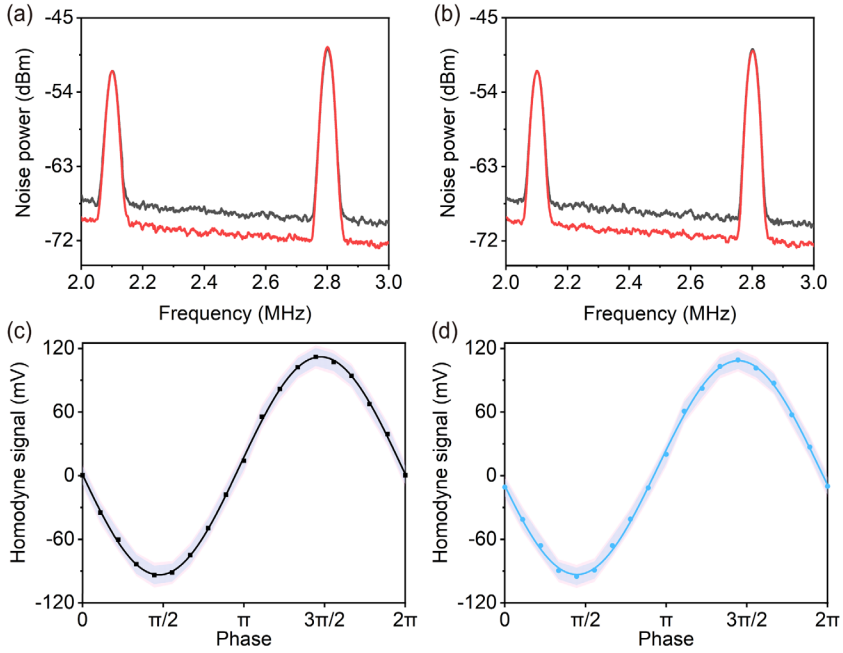

Fig. 4. (a, b) Experimental results of the individual measurement power spectra of the vibration of ultrasonic signal d at 2.1 MHz and the phase of radio frequency signal θ at 2.8 MHz at the first sensor (a) and the second sensor (b). The black and red traces correspond to the noise power based on classical and entangled schemes, respectively. (c, d) The radio frequency phases at the first and second sensors extracted from the jointly processed detection outputs of BHD2 and BHD3.

that the entangled sensing network for individual measurement achieves a reduced estimation variance of 2.5 dB below the SQL.

To quantify the high sensitivity for distributed quantum sensing of multimodal parameters, the relationship between sensitivity and the ultimate limit of the quantum sensing network is investigated. Figure 5(a)–5(c) show the sensitivities for amplitude and phase of radio frequency signals and amplitude of ultrasonic signals as a function of phase-sensing powers, respectively. They reveal a clear improvement of sensitivities with higher phase-sensing power. Particularly, QFI describes the phase-sensing potential of quantum state in network, which gives the sensitivity limit of the QCRB (dashed trace). For the Gaussian states, QFI can be obtained based on the mean values and covariance matrix of optical fields, which can be measured by the BHD. We observe that the QFI is 1.83×10^{16} from the squeezing factor $r = 0.46$ in the experiment, and the QFI-related sensitivities can be increased to approach the QCRB with an increase in the squeezing factor (theoretical calculations of the QCRB are provided in Supplement 1). The sensitivity can be brought closer to the QCRB by further reducing all losses (dotted-dashed trace). Therefore, such a quantum network enables both joint and individual measurements of the amplitude and phase of multiple radio frequency signals, as well as the vibrations of multiple ultrasonic signals.

4. DISCUSSION AND OUTLOOK

In conclusion, we have proposed and demonstrated a high-sensitivity distributed quantum sensing scheme in a CV GHZ entangled network, where multimodal parameters can be sensed beyond the SQL. Beyond a single type of parameter [28,30,31,34], the multimodal parameters include the multiple radio frequency amplitude and phase signals as well as the multiple ultrasonic vibration signals. The GHZ state across multiple modes allows

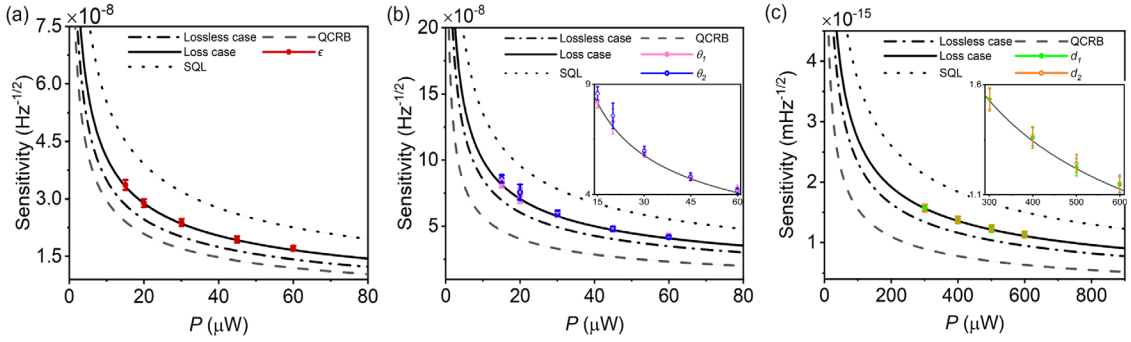

Fig. 5. Sensitivities of (a) the averaged amplitude of radio frequency signals ϵ_1^J, (b) the phases of radio frequency signals θ_1 and θ_2, and (c) the vibrations of ultrasonic signals d_1 and d_2 as a function of phase-sensing powers. The solid and dotted-dashed traces represent the sensitivities calculated under lossy and lossless conditions, respectively. The dotted and dashed traces denote the SQL and QCRB. The measured sensitivities for different measured observables are indicated by circles of different colors: red for ϵ_1^J, pink for θ_1, blue for θ_2, green for d_1, and orange for d_2. All error bars are ± standard deviation.

not only joint but also individual measurements of multimodal parameters beyond the SQL, where the measurement information can be qualitatively increased by simultaneously reading out two conjugate parameters. Particularly, the quadrature sensitivity is improved from the order of 10^{-2} [28,30] to that of 10^{-8}, by exploiting MZIs to couple high-power lasers with the GHZ entangled state. Future developments are expected to integrate more entangled modes with adaptive optical strategies, thereby paving the way for practical applications in multimodal generative AI [42], multimodal brain–computer interfaces [44], and spectroscopy [57].

Funding. Innovation Program for Quantum Science and Technology (2024ZD0300900); National Natural Science Foundation of China (62122044, 61925503, 62135008); Key Project of the National Key R & D program of China (2022YFA1404500); Fundamental Research Program of Shanxi Province (202403021223001).

Disclosures. The authors declare no conflicts of interest.

Data availability. Data underlying the results presented in this paper are not publicly available at this time but may be obtained from the authors upon reasonable request.

Supplemental document. See Supplement 1 for supporting content.

REFERENCES

1. L. Pezzè, A. Smerzi, M. K. Oberthaler, *et al.*, "Quantum metrology with nonclassical states of atomic ensembles," Rev. Mod. Phys. **90**, 035005 (2018).
2. T. Nagata, R. Okamoto, J. L. O'Brien, *et al.*, "Beating the standard quantum limit with four-entangled photons," Science **316**, 726–729 (2007).
3. F. Hudelist, J. Kong, C. Liu, *et al.*, "Quantum metrology with parametric amplifier-based photon correlation interferometers," Nat. Commun. **5**, 3049 (2014).
4. M. Manceau, G. Leuchs, F. Khalili, *et al.*, "Detection loss tolerant supersensitive phase measurement with an SU(1,1) interferometer," Phys. Rev. Lett. **119**, 223604 (2017).
5. S. Daryanoosh, S. Slussarenko, D. W. Berry, *et al.*, "Experimental optical phase measurement approaching the exact Heisenberg limit," Nat. Commun. **9**, 4606 (2018).
6. J. Qin, Y. H. Deng, H. S. Zhong, *et al.*, "Unconditional and robust quantum metrological advantage beyond NOON states," Phys. Rev. Lett. **130**, 070801 (2023).
7. J. Aasi, J. Abadie, B. P. Abbott, *et al.*, "Enhanced sensitivity of the LIGO gravitational wave detector by using squeezed states of light," Nat. Photonics **7**, 613–619 (2013).
8. M. Tse, H. Yu, N. Kijbunchoo, *et al.*, "Quantum-enhanced advanced LIGO detectors in the era of gravitational-wave astronomy," Phys. Rev. Lett. **123**, 231107 (2019).
9. X. Zuo, Z. Yan, Y. Feng, *et al.*, "Quantum interferometer combining squeezing and parametric amplification," Phys. Rev. Lett. **124**, 173602 (2020).
10. J. Yu, Y. Qin, J. Qin, *et al.*, "Quantum enhanced optical phase estimation with a squeezed thermal state," Phys. Rev. Appl. **13**, 024037 (2020).
11. L. O. D. Collaboration, D. Ganapathy, W. Jia, *et al.*, "Broadband quantum enhancement of the LIGO detectors with frequency-dependent squeezing," Phys. Rev. X **13**, 041021 (2023).
12. J. Südbeck, S. Steinlechner, M. Korobko, *et al.*, "Demonstration of interferometer enhancement through Einstein–Podolsky–Rosen entanglement," Nat. Photonics **14**, 240–244 (2020).
13. S. Wu, G. Bao, J. Guo, *et al.*, "Quantum magnetic gradiometer with entangled twin light beams," Sci. Adv. **9**, eadg1760 (2023).
14. Y. Israel, S. Rosen, and Y. Silberberg, "Supersensitive polarization microscopy using NOON states of light," Phys. Rev. Lett. **112**, 103604 (2014).
15. Z. Hou, H. Zhu, G. Y. Xiang, *et al.*, "Achieving quantum precision limit in adaptive qubit state tomography," npj Quantum Inf. **2**, 16001 (2016).
16. T. Baumgratz and A. Datta, "Quantum enhanced estimation of a multidimensional field," Phys. Rev. Lett. **116**, 030801 (2016).
17. L. A. Lugiato, A. Gatti, and E. Brambilla, "Quantum imaging," J. Opt. B: Quantum Semiclass. Opt. **4**, S176 (2002).
18. J. P. Dowling and K. P. Seshadreesan, "Quantum optical technologies for metrology, sensing, and imaging," J. Lightwave Technol. **33**, 2359–2370 (2015).
19. F. Albarelli, M. Barbieri, M. G. Genoni, *et al.*, "A perspective on multiparameter quantum metrology: from theoretical tools to applications in quantum imaging," Phys. Lett. A **384**, 126311 (2020).
20. H. Defienne, W. P. Bowen, M. Chekhova, *et al.*, "Advances in quantum imaging," Nat. Photonics **18**, 1024–1036 (2024).
21. M. A. Taylor, J. Janousek, V. Daria, *et al.*, "Biological measurement beyond the quantum limit," Nat. Photonics **7**, 229–233 (2013).
22. M. A. Taylor and W. P. Bowen, "Quantum metrology and its application in biology," Phys. Rep. **615**, 1–59 (2016).
23. N. Aslam, H. Zhou, E. K. Urbach, *et al.*, "Quantum sensors for biomedical applications," Nat. Rev. Phys. **5**, 157–169 (2023).
24. B. K. Malia, Y. Wu, J. Martínez-Rincón, *et al.*, "Distributed quantum sensing with mode-entangled spin-squeezed atomic states," Nature **612**, 661–665 (2022).
25. P. Kómár, E. M. Kessler, M. Bishof, *et al.*, "A quantum network of clocks," Nat. Phys. **10**, 582–587 (2014).
26. M. Gessner, A. Smerzi, and L. Pezzè, "Multiparameter squeezing for optimal quantum enhancements in sensor networks," Nat. Commun. **11**, 3817 (2020).
27. Q. Zhuang, Z. Zhang, and J. H. Shapiro, "Distributed quantum sensing using continuous-variable multipartite entanglement," Phys. Rev. A **97**, 032329 (2018).
28. X. Guo, C. R. Breum, J. Borregaard, *et al.*, "Distributed quantum sensing in a continuous-variable entangled network," Nat. Phys. **16**, 281–284 (2020).
29. S. Hong, J. ur Rehman, Y. S. Kim, *et al.*, "Quantum enhanced multiple-phase estimation with multi-mode *N*00*N* states," Nat. Commun. **12**, 5211 (2021).
30. D. H. Kim, S. Hong, Y. S. Kim, *et al.*, "Distributed quantum sensing of multiple phases with fewer photons," Nat. Commun. **15**, 266 (2024).
31. L. Z. Liu, Y. Z. Zhang, Z. D. Li, *et al.*, "Distributed quantum phase estimation with entangled photons," Nat. Photonics **15**, 137–142 (2021).
32. S. R. Zhao, Y. Z. Zhang, W. Z. Liu, *et al.*, "Field demonstration of distributed quantum sensing without post-selection," Phys. Rev. X **11**, 031009 (2021).
33. Z. Zhang and Q. Zhuang, "Distributed quantum sensing," Quantum Sci. Technol. **6**, 043001 (2021).
34. Y. Xia, W. Li, W. Clark, *et al.*, "Demonstration of a reconfigurable entangled radio-frequency photonic sensor network," Phys. Rev. Lett. **124**, 150502 (2020).
35. S. Duan, Q. Shi, and J. Wu, "Multimodal sensors and ML-based data fusion for advanced robots," Adv. Intell. Syst. **4**, 2200213 (2022).
36. R. Yang, W. Zhang, N. Tiwari, *et al.*, "Multimodal sensors with decoupled sensing mechanisms," Adv. Sci. **9**, 2202470 (2022).
37. J. N. Acosta, G. J. Falcone, P. Rajpurkar, *et al.*, "Multimodal biomedical AI," Nat. Med. **28**, 1773–1784 (2022).
38. Q. Mao, Z. Liao, J. Yuan, *et al.*, "Multimodal tactile sensing fused with vision for dexterous robotic housekeeping," Nat. Commun. **15**, 6871 (2024).
39. F. Yu, Y. Wu, S. Ma, *et al.*, "Brain-inspired multimodal hybrid neural network for robot place recognition," Sci. Robot. **8**, eabm6996 (2023).
40. A. Mecozzi, M. Cantono, J. C. Castellanos, *et al.*, "Polarization sensing using submarine optical cables," Optica **8**, 788–795 (2021).
41. G. Marra, D. M. Fairweather, V. Kamalov, *et al.*, "Optical interferometry–based array of seafloor environmental sensors using a transoceanic submarine cable," Science **376**, 874–879 (2022).
42. V. M. Rao, M. Hla, M. Moor, *et al.*, "Multimodal generative AI for medical image interpretation," Nature **639**, 888–896 (2025).
43. X. Sheng, Y. Sui, L. Li, *et al.*, "Multimodal technologies for neural modulation and sensing," Fundam. Res. **5**, 1–2 (2025).
44. S. Pancholi and A. M. Joshi, "Electromyography-based hand gesture recognition system for upper limb amputees," IEEE Sens. Lett. **3**, 5500304 (2019).
45. A. J. Brady, C. Gao, R. Harnik, *et al.*, "Entangled sensor-networks for dark-matter searches," PRX Quantum **3**, 030333 (2022).
46. M. Jiang, T. Hong, D. Hu, *et al.*, "Long-baseline quantum sensor network as dark matter haloscope," Nat. Commun. **15**, 3331 (2024).
47. B. Xia, J. Huang, H. Li, *et al.*, "Toward incompatible quantum limits on multiparameter estimation," Nat. Commun. **14**, 1021 (2023).

48. M. D. Vidrighin, G. Donati, M. G. Genoni, *et al.*, "Joint estimation of phase and phase diffusion for quantum metrology," Nat. Commun. **5**, 3532 (2014).
49. V. Novikov, J. Jia, T. B. Brasil, *et al.*, "Hybrid quantum network for sensing in the acoustic frequency range," Nature **643**, 955–960 (2025).
50. H. Wu, G. D. Mitts, C. Z. C. Ho, *et al.*, "Wideband electric field quantum sensing via motional Raman transitions," Nat. Phys. **21**, 380–385 (2025).
51. C. Fabre and N. Treps, "Modes and states in quantum optics," Rev. Mod. Phys. **92**, 035005 (2020).
52. S. Liang, J. Cheng, J. Qin, *et al.*, "High-speed quantum radio-frequency-over-light communication," Phys. Rev. Lett. **132**, 140802 (2024).
53. J. Cheng, S. Liang, J. Qin, *et al.*, "Semi-device-independent quantum random number generator with a broadband squeezed state of light," npj Quantum Inf. **10**, 20 (2024).
54. Y. Zhou, J. Yu, Z. Yan, *et al.*, "Quantum secret sharing among four players using multipartite bound entanglement of an optical field," Phys. Rev. Lett. **121**, 150502 (2018).
55. S. Steinlechner, J. Bauchrowitz, M. Meinders, *et al.*, "Quantum-dense metrology," Nat. Photonics **7**, 626–630 (2013).
56. M. Ast, S. Steinlechner, and R. Schnabel, "Reduction of classical measurement noise via quantum-dense metrology," Phys. Rev. Lett. **117**, 180801 (2016).
57. H. Hainzer, D. Kiesenhofer, T. Ollikainen, *et al.*, "Correlation spectroscopy with multiqubit-enhanced phase estimation," Phys. Rev. X **14**, 011033 (2024).